Inorg. Chem. **2007**, *46*, 2988–2997

Structural and Magnetic Properties of Layered Copper(II) Coordination Polymers Intercalating s and f Metal Ions

Jorge A. R. Navarro,*,† Elisa Barea,† Juan M. Salas,† Norberto Masciocchi,‡ Simona Galli,*,‡ and Angelo Sironi§

Departamento de Química Inorgánica, Universidad de Granada, Av. Fuentenueva S/N, 18071 Granada, Spain, Dipartimento di Scienze Chimiche e Ambientali, Università dell'Insubria, Via Valleggio 11, 22100 Como, Italy, and Dipartimento di Chimica Strutturale e Stereochimica Inorganica, Università di Milano via Venezian 21 and CIMAINA, Via Celoria 16, 20133 Milano, Italy

Received July 25, 2006

The nanoporous coordination polymer [Cu(pyrimidin-2-olate-*N*1,*N*3)$_2$]$_n$ (**1$_C$**) of the sodalite zeotype sorbs a variety of metal nitrates [M(NO$_3$)$_m$, M = Na$^+$, K$^+$, Rb$^+$, Tl$^+$, Ca^{2+}, Sr^{2+}, Ba^{2+}, Pb^{2+}, La^{3+}, Nd^{3+}, Gd^{3+}, Er^{3+}] from H$_2$O/MeOH solutions, with a concomitant structural change to a *layered* [Cu(pyrimidin-2-olate-*N*1,*N*3)$_2$]$_n$·[M(NO$_3$)$_m$]$_{n/2}$ (**MNO$_3$@1$_L$**) coordination framework. Single-crystal X-ray diffraction analyses revealed that the layers are based on Cu$_4$(pyrimidin-2-olate-*N*1,*N*3)$_4$ square grids of copper(II) ions bridged by *N*1,*N*3 exobidentate ligands, displaying a structural motif of the metallacalix[4]arene type in pinched cone conformation. The interlayer space is occupied by the guest metal nitrates, each metal being coordinated by (at least) the four oxygen atoms of a metallacalix[4]arene. Magnetic measurements on the **MNO$_3$@1$_L$** series denoted a weak ferromagnetic ordering taking place below the Néel temperatures (typically close to 35 K), arising from spin-canting phenomena of the antiferromagnetically coupled copper centers. When M = Nd^{3+}, Gd^{3+}, or Er^{3+}, additional magnetic ordering is observed at lower temperatures, which, on the basis of static and dynamic magnetic susceptibility measurements, can be attributed to copper–lanthanide interactions.

Introduction

The large anisotropic magnetic moment of lanthanides (Ln) has attracted great interest in the search for hard molecular magnets.[1−3] Accordingly, different types of lanthanide-containing molecular magnets have been investigated, which can be classified into two main types of systems: polynuclear materials in which the spin carriers are Ln ions[1] and materials in which the lanthanide ion is coupled to a second spin carrier, such as organic radicals[2,4] or transition-metal ions.[5] The magnetic properties of these systems will be dominated by two phenomena, the first one arising from the intrinsic nature of the Ln ion (originating from the thermal population of the Stark sublevels) and the second one as a result of the exchange interaction between the different magnetic centers.[6]

We recently reported[7] the ability of the (hydrated) distorted sodalitic [Cu(2-pymo-*N*1,*N*3)$_2$]$_n$ framework (**1$_R$**) (2-pymo = pyrimidin-2-olate) to incorporate MX ion pairs through heterogeneous solid−liquid processes responsible for crystal-

* To whom correspondence should be addressed. E-mail: jarn@ugr.es (J.A.R.N.), simona.galli@uninsubria.it (S.G.).
† Universidad de Granada.
‡ Università dell'Insubria.
§ Università di Milano and CIMAINA.

(1) (a) Hatscher, S. T.; Urland, W. *Angew. Chem., Int. Ed.* **2003**, *42*, 2862. (b) Zhang, Z.-H.; Okamura, T.-A.; Hasegawa, Y.; Kawaguchi, H.; Kong, L.-Y.; Sun, W.-Y.; Ueyama, N. *Inorg. Chem.* **2005**, *44*, 6219.
(2) Kahn, M. L.; Ballou, R.; Porcher, P.; Kahn, O.; Sutter, J.-P. *Chem.—Eur. J.* **2002**, *8*, 525.
(3) (a) Costes, J.-P.; Dahan, F.; Wernsdorfer, W. *Inorg. Chem.* **2006**, *45*, 5. (b) Osa, S.; Kido, T.; Matsumoto, N.; Re, N.; Pochaba, A. *J. Am. Chem. Soc.* **2004**, *126*, 420. (c) Zaleski, C. M.; Depperman, E. C.; Kampf, J. W.; Kirk, M. L.; Pecoraro, V. *Angew. Chem., Int. Ed.* **2004**, *43*, 3912. (d) Ishikawa, N.; Sugita, M.; Ishikawa, T.; Koshihara, S.; Kaizu, Y. *J. Am. Chem. Soc.* **2003**, *125*, 8694.
(4) Bernot, K.; Bogani, L.; Caneschi, A.; Gatteschi, D.; Sessoli, R. *J. Am. Chem. Soc.* **2006**, *128*, 7947.
(5) (a) Benelli, C.; Blake, A. J.; Milne, P. E. Y.; Rawson, J. M.; Winpenny, R. E. P. *Chem.—Eur. J.* **1995**, *1*, 614. (b) Bencini, A.; Benelli, C.; Caneschi, A.; Carlin, R. L.; Dei, A.; Gatteschi, D. *J. Am. Chem. Soc.* **1985**, *107*, 8128. (c) Costes, J. P.; Clemente-Juan, J. M.; Dahan, F.; Dumestre, F.; Touchages, J.-P. *Inorg. Chem.* **2002**, *41*, 2886.
(6) *Lanthanide Probes in Life, Chemical and Earth Sciences: Theory and Practice*; Bünzli, J. C. G., Chopin, G. R., Eds.; Elsevier: Amsterdam, 1989.
(7) Barea, E.; Navarro, J. A. R.; Salas, J. M.; Masciocchi, N.; Galli, S.; Sironi, A. *J. Am. Chem. Soc.* **2004**, *126*, 3014.

10.1021/ic061384i CCC: $37.00
Published on Web 03/20/2007

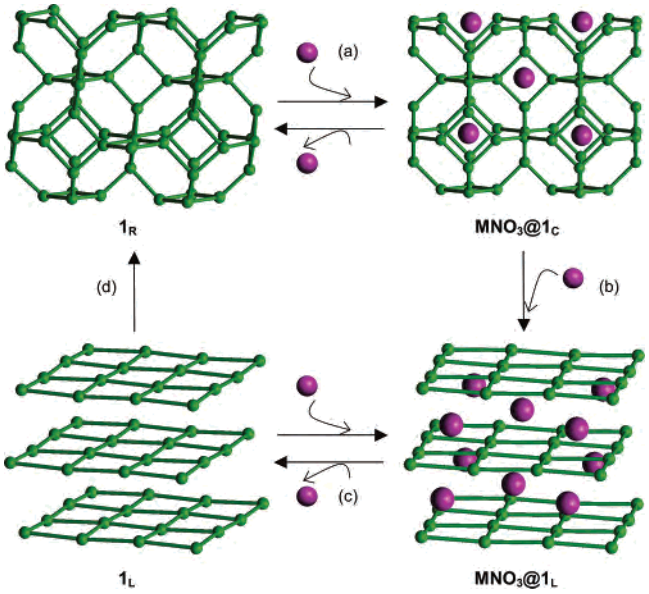

Figure 1. Guest-induced transformations in the $[Cu(2\text{-pymo-}N1,N3)_2]_n$ (**1_R**) framework: (a) incorporation of $^n/_3M(NO_3)_m$, (b) additional incorporation of $^n/_6M(NO_3)_m$, (c) removal of $^n/_2M(NO_3)_m$, and (d) water addition. Green and purple balls and sticks denote Cu, $M(NO_3)_m$, and 2-pymo-*N*1,*N*3-bridges, respectively.

to-crystal phase transitions (Figure 1). The latter, induced by the guest ionic couples, strictly depend both on their nature and on the polarity of the liquid phase. In the presence of solvents with reduced polarity (water/methanol or water/ethanol solutions), adsorption selectivity toward nitrate salts has been proved, which promotes a phase transition from the distorted trigonal **1_R** species to the undistorted cubic $[Cu(2\text{-pymo-}N1,N3)_2]_n\cdot(MNO_3)_{n/3}$ one (**$MNO_3@1_C$**, M = Li^+ or NH_4^+). As will be substantiated below, a further structural change from **$MNO_3@1_C$** to a layered $[Cu(2\text{-pymo-}N1,N3)_2]_n\cdot[M(NO_3)_m]_{n/2}$ material (**$MNO_3@1_L$**), with the $M(NO_3)_m$ guests occupying the interlayer space, has been achieved with cations having dimensions equal to or greater than Na^+ (r_{Na+} = 1.18 Å, for coordination number 8).[8]

To verify the flexibility of the **1_R** framework and its inclusion properties further, a variety of s-, p-, and f-block metal ion nitrates [$M(NO_3)_m$, M = Na^+, K^+, Rb^+, Tl^+, Ca^{2+}, Sr^{2+}, Ba^{2+}, Pb^{2+}, La^{3+}, Nd^{3+}, Gd^{3+}, Er^{3+}] have been employed. The resulting heterometallic phases, characterized by X-ray single crystal and powder diffraction methods, thermal analysis, and variable-temperature magnetic measurements, are described hereafter. The heterogeneous synthetic strategy adopted for the preparation of these heterometallic complexes clearly differs from the classical approaches using metal ligand precursors in the homogeneous phase.[9]

As shown in the following sections, the obtained materials, although being structurally related, do not always afford single crystals or polycrystalline species of suitable quality to allow a complete structural characterization. Nevertheless, the coupling of diffraction analyses on a few monocrystals with conventional X-ray powder diffraction (XRPD) measurements allowed us to unravel the structural rules governing these inclusion processes, which could then be traced back to the physicochemical properties of the distinct guest metal ions.

Experimental Section

Materials. 2-Hydroxypyrimidine·HCl was purchased from Aldrich. The rhombohedral form of $[Cu(2\text{-pymo-}N1,N3)_2]_n\cdot nH_2O$ (**1_R**) was prepared as previously reported.[10]

Preparation of $[Cu(2\text{-pymo})_2]\cdot(M(NO_3)_m)_{1/2}$ ($MNO_3@1_L$), M = Na^+, K^+, Rb^+, Tl^+, Be^{2+}, Mg^{2+}, Ca^{2+}, Sr^{2+}, Ba^{2+}, Pb^{2+}, La^{3+}, Nd^{3+}, Gd^{3+}, Er^{3+}. These brown microcrystalline solids were obtained by stirring a suspension of **1_R** (150 mg) in a 0.05 M solution of the corresponding nitrate salt in 25 mL of a water/methanol (1:4) mixture. The thermodynamic equilibrium is reached at different periods of time ranging from 24 h for M = La^{3+} to 7 days for M = Tl^+ and K^+. To ensure that the thermodynamic equilibrium was achieved, we have exposed all of the samples to the salt solution for 1 week at room temperature. In the case of M = Ba^{2+}, it should be noted that no intermediate formation of a cubic phase is observed.

Crystals of **$MNO_3@1_L$**, with M = K^+, Rb^+, Tl^+, suitable for X-ray analysis were grown from an ammonia/water/methanol (2:11:7) solution (25 mL) containing $Cu(NO_3)_2\cdot 3H_2O$ (2 mmol), 2-hydroxypyrimidine·HCl (4 mmol), and MNO_3 (1 mmol). Brown crystals of **$MNO_3@1_L$** were obtained after a few days.

Elemental Analyses. $NaNO_3@1_L$: Yield 100%. Anal. Calcd for $C_8H_6CuNa_{0.50}N_{4.50}O_{3.50}\cdot(CH_3OH)\cdot(H_2O)$: C, 31.78; H, 2.82; N, 19.62. Found: C, 31.4; H, 2.5; N, 19.6.

$KNO_3@1_L$: Yield 100%. Anal. Calcd for $C_8H_6CuK_{0.50}N_{4.50}O_{3.50}\cdot 0.5(CH_3OH)\cdot 0.5(H_2O)$: C, 31.00; H, 2.75; N, 19.14. Found: C, 31.2; H, 2.8; N, 19.5. UV−vis, nm: 295 (vs), 330 (vs, sh), 500 (s), 640 (s, sh).

$RbNO_3@1_L$: Yield 100%. Anal. Calcd for $C_8H_6CuRb_{0.50}N_{4.50}O_{3.50}\cdot(CH_3OH)\cdot(H_2O)$: C, 28.97; H, 2.57; N, 17.88. Found: C, 29.0; H, 2.6; N, 18.0. UV−vis, nm: 290 (vs), 335 (vs, sh), 500 (s), 640 (s, sh).

$TlNO_3@1_L$: Yield 100%. Anal. Calcd for $C_8H_6CuTl_{0.40}N_{4.40}O_{3.20}\cdot 0.4(CH_3OH)\cdot 0.4(H_2O)$: C, 26.53; H, 2.49; N, 16.21. Found: C, 26.1; H, 3.5; N, 16.5.

$Be(NO_3)_2@1_L$: Yield 100%. Anal. Calcd for $C_8H_6CuBe_{0.50}N_5O_5\cdot 0.5(CH_3OH)\cdot 0.5(H_2O)$: C, 29.57; H, 2.62; N, 20.29. Found: C, 29.4; H, 2.7; N, 20.4.

$Mg(NO_3)_2@1_L$: Yield 100%. Anal. Calcd for $C_8H_6CuMg_{0.50}N_5O_5\cdot 0.5(CH_3OH)\cdot 0.5(H_2O)$: C, 28.93; H, 2.57; N, 19.85. Found: C, 28.7; H, 2.7; N, 19.9.

$Ca(NO_3)_2@1_L$: Yield 100%. Anal. Calcd for $C_8H_6CuCa_{0.50}N_5O_5\cdot 0.4(CH_3OH)\cdot 0.4(H_2O)$: C, 27.71; H, 2.32; N, 20.00. Found: C, 27.6; H, 2.2; N, 19.9.

$Sr(NO_3)_2@1_L$: Yield 100%. Anal. Calcd for $C_8H_6CuSr_{0.7}N_{5.4}O_{6.2}\cdot 0.5(CH_3OH)\cdot 0.5(H_2O)$: C, 23.91; H, 2.13; N, 17.71. Found: C, 26.5; H, 2.6; N, 16.4.

$Ba(NO_3)_2@1_L$: Yield 100%. Anal. Calcd for $C_8H_6CuBa_{0.50}N_5O_5\cdot 0.5(CH_3OH)\cdot 0.5(H_2O)$: C, 24.93; H, 2.22; N, 17.11. Found: C, 24.8; H, 2.3; N, 17.0.

$Pb(NO_3)_2@1_L$: Yield 100%. Anal. Calcd for $C_8H_6CuPb_{0.50}N_5O_5\cdot 0.1(CH_3OH)\cdot(H_2O)$: C, 22.08; H, 1.92; N, 15.90 Found: C, 21.8; H, 1.9; N, 15.7.

(8) Shannon, R. D. *Acta Crystallogr.* **1976**, *A32*, 751.
(9) (a) Navarro, J. A. R.; Salas, J. M. *Chem. Commun.* **2000**, 235. (b) Kitagawa, S.; Noro, S.-I.; Nakamura, T. *Chem. Commun.* **2006**, 701. (c) Rodriguez, A.; Sakiyama, H.; Masciocchi, N.; Galli, S.; Galvez, N.; Lloret, F.; Colacio, E. *Inorg. Chem.* **2005**, *44*, 8399.
(10) Tabares, L. C.; Navarro, J. A. R.; Salas, J. M. *J. Am. Chem. Soc.* **2001**, *123*, 383.

$La(NO_3)_3@1_L$: Yield 100%. Anal. Calcd for $C_8H_6CuLa_{0.50}N_{5.50}O_{6.50}\cdot 0.25(CH_3OH)\cdot 0.25(H_2O)$: C, 23.16; H, 2.04; N, 17.48. Found: C, 23.1; H, 1.8; N, 17.2.

$Er(NO_3)_3@1_L$: Yield 100%. Anal. Calcd for $C_8H_6CuEr_{0.50}N_{5.50}O_{6.50}\cdot 0.17(CH_3OH)\cdot 0.17(H_2O)$: C, 22.36; H, 1.61; N, 17.56. Found: C, 22.4; H, 1.7; N, 17.6.

$Gd(NO_3)_3@1_L$: Yield 100%. Anal. Calcd for $C_8H_6CuGd_{0.50}N_{5.50}O_{6.50}\cdot 0.5(CH_3OH)$: C, 23.13; H, 1.83; N, 17.45. Found: C, 23.5; H, 1.8; N, 17.9.

$Nd(NO_3)_3@1_L$: Yield 100%. Anal. Calcd for $C_8H_6CuNd_{0.50}N_{5.50}O_{6.50}\cdot 0.20(CH_3OH)\cdot 0.40(H_2O)$: C, 22.76; H, 1.77; N, 17.81. Found: C, 22.4; H, 1.4; N, 17.5.

Characterization and Physical Measurements. Elemental (C, H, N) analyses were obtained using a Fisons Carlo Erba EA1008 analyzer; thermogravimetric analyses were performed on a Shimadzu TGA-50H analyzer in the presence of a dinitrogen atmosphere. (All of these instruments are located at the Centre of Scientific Instrumentation of the University of Granada.) IR spectra were recorded on a Thermo Nicolet IR 200 spectrometer using KBr pellets. Magnetic susceptibility measurements were performed on polycrystalline samples in the 2−250 K range with a Quantum Design MPMS-XL SQUID in the field-cooled mode applying 100, 300, and 5000, 10 000 Oe. ac magnetic susceptibility measurements were performed in the 2−30 K range in a 1 Oe oscillating field at frequencies ranging from 1 to 1000 Hz.

Single-Crystal X-ray Diffractometry. The species **$KNO_3@1_L$**, **$RbNO_3@1_L$**, and **$TlNO_3@1_L$** crystallize as brownish single crystals suitable for X-ray diffraction. Crystals of approximately 0.05 × 0.20 × 0.20, 0.02 × 0.02 × 0.15, and 0.04 × 0.10 × 0.15 mm^3 dimensions (for **$KNO_3@1_L$**, **$RbNO_3@1_L$**, and **$TlNO_3@1_L$**, respectively) were glued on the tip of a glass fiber and mounted on top of a goniometer head. Data were collected using graphite-monochromated Mo Kα radiation on an Enraf Nonius CAD-4 (**$KNO_3@1_L$** and **$TlNO_3@1_L$**) or a Bruker AXS SMART (**$RbNO_3@1_L$**) automated diffractometer. In the case of the CAD-4 diffractometer, the unit cells were determined on the basis of the setting angles of 25 intense, randomly distributed reflections with θ in the 10−17 and 10−16° ranges (for **$KNO_3@1_L$** and **$TlNO_3@1_L$**, respectively). In the case of SMART, the unit cell was determined by acquiring 60 frames at different ω and ϕ goniometer angles. A total of 2336, 20 554, and 2221 reflections, in the $3 < \theta < 25.3°$, $2 < \theta < 22°$, and $3 < \theta < 25.3°$ ranges (for **$KNO_3@1_L$**, **$RbNO_3@1_L$**, and **$TlNO_3@1_L$**, respectively) were collected in the ω-scan mode. The data were collected for Lorenz polarization and absorption effects.[11] The structure solutions and refinements were performed by direct methods (SIR-97)[12] and full-matrix least-squares procedures on F^2 (SHELX-97),[13] respectively, as implemented in the WinGX suite of programs. All of the non-hydrogen atoms with the exception of the nitrate ions, the methanol, and the water molecules were treated anisotropically. The hydrogen atoms were constrained to ride on the pertinent parent atoms with an isotropic thermal-displacement parameter arbitrarily chosen to be 1.2 times that of the parent atom itself.

For the sake of completeness, it must be pointed out that the three species are affected by heavy disorder, which, in the initial stages of the solution process, made the choice of the space group ambiguous (in terms of the presence of a crystallographic inversion center). The disorder is such that the actual sequence of the guest molecules between the $[Cu(2\text{-pymo-}N1,N3)_2]_n$ layers may not reflect an ideal (periodic) packing. Non-negligible residual peaks (near 2 $e\cdot Å^{-3}$) are present in the difference Fourier maps in *chemically unsuitable* locations, due (at least in part) to probable polytypic sequences about the crystallographic axis perpendicular to the layers. Satellite diffraction peaks along c^* have indeed been observed, making the definition of this axis somehow uncertain. Moreover, in the case of Rb^+ and Tl^+, the *refined* site occupation factors significantly differ from unity, as if vacant sites were present. The disorder involving water molecules and nitrate ions about the M^+ ions is an additional cause of inaccuracy. The nitrate anions have been modeled by imposing equal N−O distances of 1.250(1) Å and equal, isotropic thermal displacement parameters for the oxygen atoms. As a consequence, the structural models proposed here intrinsically suffer from low accuracy and substantially represent an average image of the local environments. The final choices of the centrosymmetric space groups have been supported by carrying out multiple refinements even in the corresponding subgroups ($Pna2_1$ for **$RbNO_3@1_L$** and **$TlNO_3@1_L$**, $P2_1$ for **$KNO_3@1_L$**) and comparing the results in terms of agreement factors, model significance, and quality. Interestingly, different crystals of the *same species* could be better described by a noncentrosymmetric space group, but strong unphysical residuals about *z* still appeared (as in the centric model). We believe that this occurrence can be easily explained by a differently organized sequence of layers in an aperiodic polytypic crystal. Further details of the crystal structure analyses can be found in Table 2.

Crystallographic data (excluding structure factors) for the species **$KNO_3@1_L$**, **$RbNO_3@1_L$**, and **$TlNO_3@1_L$** have been deposited with the Cambridge Crystallographic Data Centre, supplementary publications nos. CCDC 615 750-615 752. Copies of the data can be obtained free of charge on application to CCDC, 12 Union Road, Cambridge CB21EZ, U.K. (Fax: (+44)1223−336-033; E-mail: deposit@ccdc.cam.ac.uk).

X-ray Powder Diffraction Characterization. All of the other species, not affording single crystals of suitable quality, were studied by XRPD methods. The powders were gently ground in an agate mortar and then carefully deposited in the hollow of an aluminum sample holder equipped with a quartz zero-background plate (supplied by The Gem Dugout, Swarthmore, PA). Diffraction data were collected with graphite-monochromated Cu Kα radiation, in the 5−105° (2θ) range, on a Bruker AXS D8 θ:θ diffractometer, with generator settings of 40 kV, 40 mA and slit sizes of DS = 1.0 mm, AS = 1.0 mm, and RS = 0.2 mm. The raw data are collectively reported in Figure 9, where different crystal types are shown (as indicated by the similarity of the diffraction traces); however, the poor crystallinity of the samples prevented their full structural analyses by ab initio XRPD methods. Nevertheless, a tentative assessment of the crystal symmetry and of the lattice parameters was performed by the Le Bail method (structureless whole-powder pattern fitting), as implemented in TOPAS,[14] lowering the symmetry down to monoclinic *P* when necessary. As a typical example, the final Le Bail plot for a complex trace is given in Figure 10. A collection of the refined lattice parameters can be found in Table 3.

(11) Compounds **$KNO_3@1_L$** and **$TlNO_3@1_L$**: North, A. C. T.; Phillips, D. C.; Mathews, F. S. *Acta Crystallogr.* **1968**, *A24*, 351. Compound **$RbNO_3@1_L$**: Blessing, R. H. *Acta Crystallogr.* **1995**, *A51*, 33.

(12) Altomare, A.; Burla, M. C.; Camalli, M.; Cascarano, G. L.; Giacovazzo, C.; Guagliardi, A.; Moliterni, A. G. G.; Polidori, G.; Spagna, R. *J. Appl. Crystallogr.* **1999**, *32*, 115.

(13) Sheldrick, G. M. *SHELX-97: Program for Crystal Structure Determination*; University of Göttingen: Göttingen, Germany, 1997.

(14) *Topas-R, Bruker AXS: General Profile and Structure Analysis Software for Powder Diffraction Data.*

Table 1. Crystallographic Data and Structure Refinement Parameters for the Species $\mathbf{KNO_3@1_L}$, $\mathbf{RbNO_3@1_L}$, and $\mathbf{TlNO_3@1_L}$

species	$\mathbf{KNO_3@1_L}$	$\mathbf{RbNO_3@1_L}$ 15	$\mathbf{TlNO_3@1_L}$
method	single-crystal XRD	single-crystal XRD	single-crystal XRD
formula	$C_{8.5}H_9Cu_1K_{0.5}N_{4.5}O_{4.5}$	$C_{8.5}H_9Cu_1N_{4.5}O_{4.5}Rb_{0.5}$	$C_{8.5}H_8Cu_1N_{4.5}O_4Tl_{0.5}$
fw ($g\cdot mol^{-1}$)	329.29	352.47	402.92
T (K)	298(2)	298(2)	298(2)
λ (Å)	0.71073	0.71073	0.71073
cryst syst	monoclinic	orthorhombic	orthorhombic
space group	$P2_1/m$	$Pnam$	$Pnam$
a (Å)	10.177(7)	19.070(1)	19.044(2)
b (Å)	11.42(1)	11.0596(8)	11.037(1)
c (Å)	11.033(3)	11.4266(9)	11.451(3)
β (deg)	110.72(5)	90	90
V (Å^3)	1199(1)	2409.9(3)	2406.9(7)
Z	4	8	8
ρ(calcd) ($mg\cdot m^{-3}$)	1.824	1.943[a]	2.224[a]
μ (mm^{-1})	2.02	3.84[a]	8.49[a]
F(000)	664	1400[a]	1536[a]
sample size (mm^3)	0.05 × 0.20 × 0.20	0.02 × 0.02 × 0.15	0.04 × 0.10 × 0.15
θ range (deg)	3−25	2−22	3−25
collected hkl	$0 \le h \le 12$ $0 \le k \le 13$ $-13 \le l \le 12$	$-20 \le h \le 20$ $-11 \le k \le 11$ $-12 \le l \le 12$	$0 \le h \le 22$ $0 \le k \le 13$ $0 \le l \le 13$
meas/reflns	2336/2208	20554/1674	2221/2221
absorption corr	empirical	empirical	empirical
refinement method	full-matrix least squares on F^2	full-matrix least squares on F^2	full-matrix least squares on F^2
data/restr/params	2208/3/177	1674/3/162	2221/3/168
$S(F^2)$[b]	1.211	1.111	1.073
$R(F^2)$, wR(F^2) > $2\sigma I$[a]	0.088, 0.213	0.079, 0.208	0.062, 0.142
max/min $\Delta\rho$ ($e\cdot Å^{-3}$)	2.82, −0.62[c]	2.56, −1.14[c]	1.74, −2.46[c]

[a] Calculated by admitting formal unity site occupation factors for Rb^+ and Tl^+ nitrates. [b] $S(F^2) = [\Sigma w(F_o^2 - F_c^2)^2/(n-p)]^{1/2}$ where n is the number of reflections, p is the number of parameters, and $w = 1/[\sigma^2(F_o^2) + (0.019P)^2 + 1.88P]$ with $P = (F_o^2 + 2F_c^2)/3$. $R(F) = \Sigma||F_o| - |F_c||/\Sigma|F_o|$ and wR(F^2) = $[\Sigma w(F_o^2 - F_c^2)^2/\Sigma wF_o^4]^{1/2}$. [c] See Experimental Section for a detailed explanation of such non-negligible values.

Table 2. Significant Bond Distances (Angstroms) and Angles (deg) in the Species $\mathbf{KNO_3@1_L}$, $\mathbf{RbNO_3@1_L}$, and $\mathbf{TlNO_3@1_L}$

params	$\mathbf{KNO_3@1_L}$	$\mathbf{RbNO_3@1_L}$	$\mathbf{TlNO_3@1_L}$
Cu−N	1.979(7), 2.000(7), 1.994(7), 2.000(7)	1.99(1), 1.98(1), 2.00(1), 2.00(1)	1.99(1), 1.99(1), 2.00(1), 2.01(1)
N−Cu−N	N31−Cu1−N31, 180.0 N31−Cu1−N11, 91.2(3) N11−Cu1−N11, 180.0 N21−Cu2−N21, 180.0 N21−Cu2−N13, 90.2(3) N13−Cu2−N13, 180.0	N21−Cu1−N13, 88.3(4) N21−Cu1−N11, 90.8(4) N13−Cu1−N11, 177.1(4) N21−Cu1−N31, 178.7(4) N13−Cu1−N31, 90.6(4) N11−Cu1−N31, 90.2(4)	N31−Cu1−N21, 178.2(4) N31−Cu1−N11, 90.4(4) N21−Cu1−N11, 90.6(4) N31−Cu1−N13, 88.6(4) N21−Cu1−N13, 90.4(4) N11−Cu1−N13, 176.4(4)
M−O_{pymo}	2.650(9), 2.658(9), 2.761(7)	2.77(1), 2.78(1), 2.891(8)	2.71(1), 2.75(1), 2.84(1)
M−O_{NO_3}	2.80(2), 2.92(2), 3.98(2)	3.02(3), 3.13(3), 3.41(3)	3.14(3), 3.18(3), 3.65(3)
M−O_{H_2O}	3.13(2)	3.06(3)	
Cu···M	4.39, 4.42	4.52, 4.52	4.46, 4.47

Results and Discussion

Synthesis and Thermal Properties of the $\mathbf{MNO_3@1_L}$ Species. When the (hydrated) distorted sodalitic [Cu(2-pymo-*N*1,*N*3)$_2$]$_n$ framework ($\mathbf{1_R}$) is exposed to a water/methanol or water/ethanol solution of $M(NO_3)_m$ salts (M = NH_4^+, Li^+, Na^+, K^+, Rb^+, Tl^+, Be^{2+}, Mg^{2+}, Ca^{2+}, Sr^{2+}, Ba^{2+}, Pb^{2+}, La^{3+}, Nd^{3+}, Gd^{3+}, Er^{3+}), a heterogeneous solid−liquid recognition process takes place, which results in the incorporation of one-third of a metal nitrate ion pair per $\mathbf{1_R}$ formula unit, with a concomitant crystal-to-crystal phase transition to the cubic [Cu(2-pymo-*N*1,*N*3)$_2$]$_n\cdot$[$M(NO_3)_m$]$_{n/3}$ undistorted sodalitic phase ($\mathbf{MNO_3@1_C}$, Figure 1). For M = Li^+,[7] NH_4^+,[7] Be^{2+}, and Mg^{2+}, this is the only structural transformation observed. For cations having dimensions equal to or greater than Na^+ (r_{Na+} = 1.18 Å, for coordination number 8), the additional incorporation of $^1/_6M(NO_3)_m$ in $\mathbf{MNO_3@1_C}$ occurs, which is responsible for a further structural change to a layered material of formula [Cu(2-pymo-*N*1,*N*3)$_2$]$_n\cdot$[$M(NO_3)_m$]$_{n/2}$ ($\mathbf{MNO_3@1_L}$),[15] with the $M(NO_3)_m$ guests occupying the interlayer space (Figure 1). It should be noted that the thermodynamic equilibrium of the formation of the $\mathbf{MNO_3@1_L}$ phases is reached at different periods of time, ranging from 24 h for M = La^{3+} to 7 days for M = Tl^+ and K^+, which might be related to the strength of the interaction between the metal ions and the exocyclic oxygens of the pyrimidinolate ligands (structural description). In general, we have observed the formation of the intermediate $\mathbf{MNO_3@1_C}$ phase well before the $\mathbf{MNO_3@1_L}$ one. Apparently, only for M = Ba^{2+} the cubic phase did not form (or went unobserved).

Upon gentle heating, all of the $\mathbf{MNO_3@1_L}$ species easily eliminate the solvent molecules (water and methanol) in a single endothermic process in the 40−100 °C range (e.g., ΔH = 9 $kJ\cdot mol^{-1}$ for $\mathbf{RbNO_3@1_L}$). Thermal decomposition

(15) Please note that in the previous communication (ref 7), layered compounds were denoted by the label $\mathbf{MNO_3@1_O}$. Moreover, with regard to the actual compound $\mathbf{RbNO_3@1_L}$ (previously labelled $\mathbf{RbNO_3@1_O}$, solved and refined in the non-centrosymmetric space group $Pna2_1$), its structure is now described in the centrosymmetric space group *Pnam*. For details, see the Experimental Section.

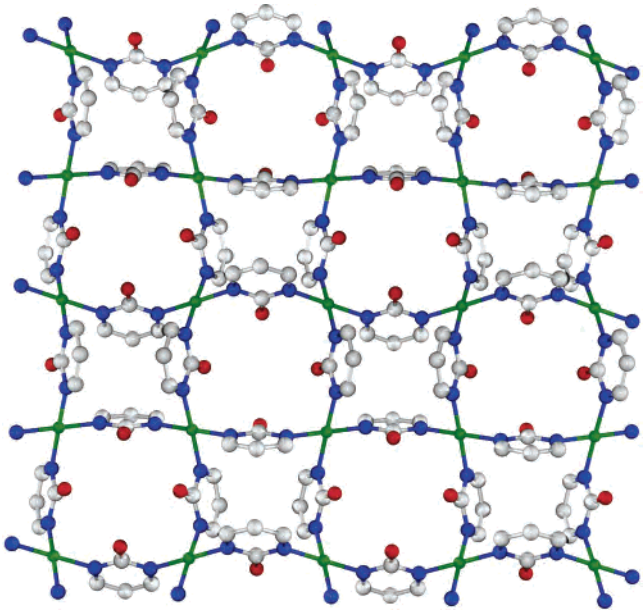

Figure 2. Representation, down [100], of one 2D $[Cu(2\text{-pymo-}N1,N3)_2]_n$ layer, of idealized *p*4/*nmm* symmetry, present in the species $\mathbf{TlNO_3@1_L}$. The layers present in $\mathbf{KNO_3@1_L}$ and $\mathbf{RbNO_3@1_L}$ are, at the drawing level, almost indistinguishable. Carbon, gray; nitrogen, blue; oxygen, red; copper, green. The hydrogen atoms have been omitted for clarity.

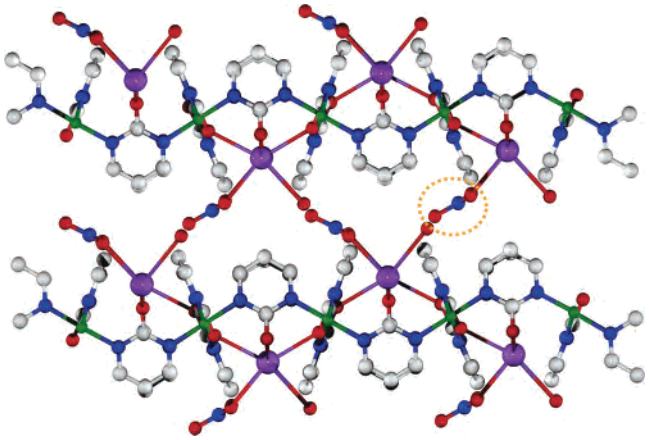

Figure 3. Representation, down [001], of the crystal packing in the species $\mathbf{KNO_3@1_L}$. Carbon, gray; nitrogen, blue; oxygen, red; copper, green; potassium, violet. For the sake of clarity, a graphical description in the non-centrosymmetric $P2_1$ space group, granting ordered nitrate and water molecules, has been adopted. With the same purpose, the hydrogen atoms and methanol molecules have been omitted. Note that the nitrate ions do not interconnect different layers, even if chelating the metal guests of a single layer (highlighted portion).

of the desolvated materials takes place at much higher temperatures, typically lying in the 260−290 °C range.

X-ray Single-Crystal Structures of the $\mathbf{MNO_3@1_L}$ Species Containing Monovalent Cations. All of the $\mathbf{MNO_3@1_L}$ species characterized by X-ray single-crystal analysis (M = K^+, Rb^+, and Tl^+) possess a 2D layered structure, defined by (nearly) square grids of formula Cu_4-(2-pymo-*N*1,*N*3)$_4$ (Figure 2). Nevertheless, whereas the orthorhombic *Pnam* $\mathbf{RbNO_3@1_L}$ and $\mathbf{TlNO_3@1_L}$ species are metrically isomorphous, $\mathbf{KNO_3@1_L}$ shows a slightly lower symmetry, that is, monoclinic $P2_1/m$. However, by applying the transformation matrix [001; 010; −201], the monoclinic cell of $\mathbf{KNO_3@1_L}$ can be traced back to an orthorhombic

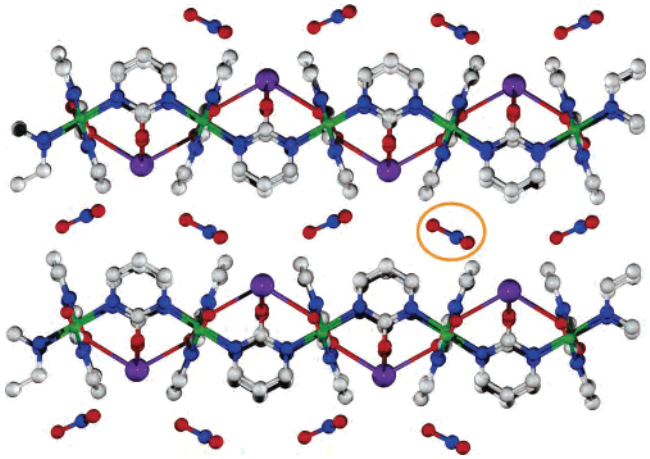

Figure 4. Representation, down [001], of the crystal packing in the species $\mathbf{RbNO_3@1_L}$. Carbon, gray; nitrogen, blue; oxygen, red; copper, green; potassium, violet. For the sake of clarity, a graphical description in the non-centrosymmetric $Pna2_1$ space group, granting ordered nitrate and water molecules, has been adopted. With the same purpose, the hydrogen atoms and methanol molecules have been omitted. Note that, in this case, the layers are interconnected by the nitrate ions (highlighted portion).

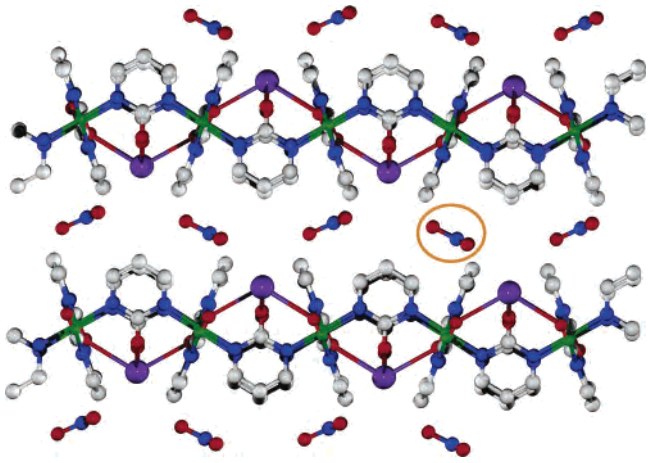

Figure 5. Representation, down [001], of the crystal packing in the species $\mathbf{TlNO_3@1_L}$. Carbon, gray; nitrogen, blue; oxygen, red; copper, green; potassium, violet. For the sake of clarity, a graphical description in the non-centrosymmetric $Pna2_1$ space group, granting ordered nitrate ions has been adopted. With the same purpose, the hydrogen atoms and methanol molecules have been omitted. In this structure, thanks to the stereochemical activity of the Tl^+ lone pair, the nitrates do not interact with them (highlighted portion).

one with $a = 11.03$, $b = 11.42$, and $c = 19.42$ Å, which compare well with the cell axes of $\mathbf{RbNO_3@1_L}$ and $\mathbf{TlNO_3@1_L}$ (Table 1) but with a β angle of 101.4°.

The asymmetric unit of the orthorhombic species contains one Cu(II) ion in a general position, half of an M ion and two half 2-pymo ligands in special locations (the crystallographic mirror plane *m*), one *complete* 2-pymo ligand in a general position, one clathrate methanol molecule possessing crystallographically imposed *m* symmetry, and half of a nitrate counterion disordered about a crystallographic inversion center (Experimental Section). In the case of the monoclinic $\mathbf{KNO_3@1_L}$ species, two half Cu(II) ions are present, but the structural description of the local geometry can be meaningfully compared with that of the Rb^+ and Tl^+ analogues. In the Rb^+ and K^+ derivatives, water molecules complete the coordination sphere of the alkaline ions.

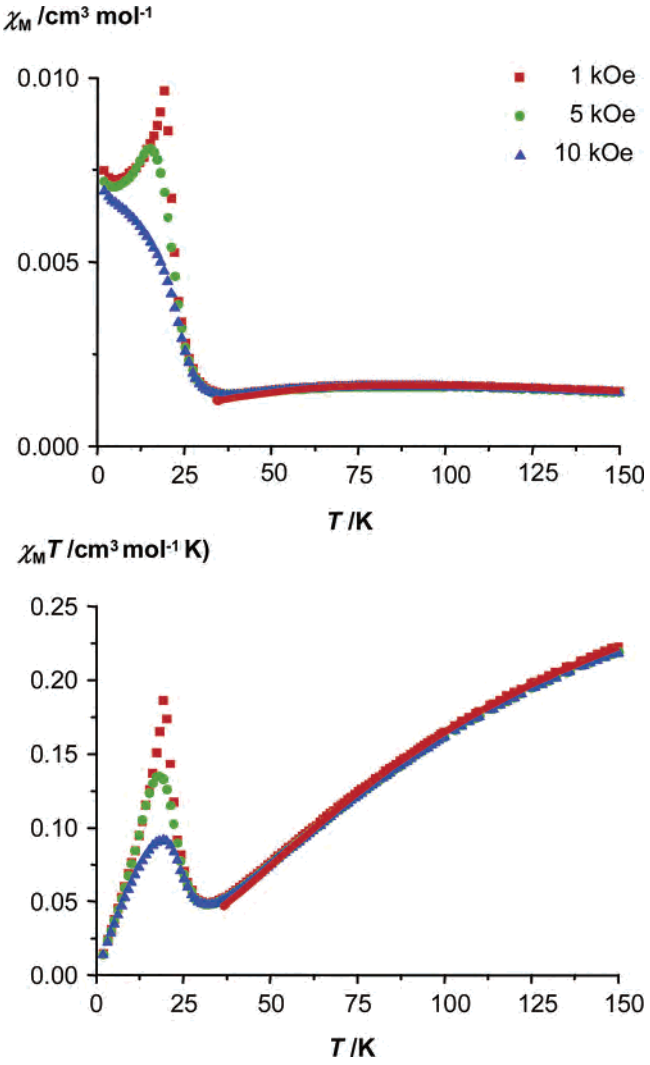

Figure 6. Field-cooled χ_M (top) and $\chi_M T$ (bottom) versus T for $\mathbf{KNO_3@1_L}$ at different field strengths. The solid red line shows the best fit of the $\chi_M T$ values to eq 1.

Each Cu(II) ion, showing very slightly distorted square-planar stereochemistry (N−Cu−N bond distances and angles, Table 2), is coordinated by one nitrogen atom of four distinct 2-pymo ligands, bridging in the usual *N*1,*N*3-exobidentate mode as already found in both the hydrated and the anhydrous forms of $[Cu(2\text{-pymo-}N1,N3)_2]_n$.[7] Because the exocyclic oxygen atoms of each $[Cu(2\text{-pymo-}N1,N3)_2]_4$ unit point toward the same direction, a metallacalix[4]arene in pinched cone conformation can be isolated. The crystallographic axes defining the $[Cu(2\text{-pymo-}N1,N3)_2]_4$ grid (in the orthorhombic phases) share similar dimensions (in the 11.03−11.46 Å range), that is, 2 × Cu···Cu, in agreement with a $[Cu(2\text{-pymo-}N1,N3)_2]_n$ layer of pseudotetragonal (*p*4/*nmm*) symmetry (Figure 2). In the monoclinic crystal (the potassium derivative), these grids have Cu···Cu edges of 5.51 and 5.70 Å, which (again) indicate the strict isostructural nature of the $[Cu(2\text{-pymo-}N1,N3)_2]_n$ layers in the different phases, irrespective of their 3D crystal system.

According to their disposition with respect to the layers, the methanol molecules and the guest metal ions belong to two distinct categories (Figures 3−5). The former are hosted within the lypophilic cavity formed by the aromatic rings of

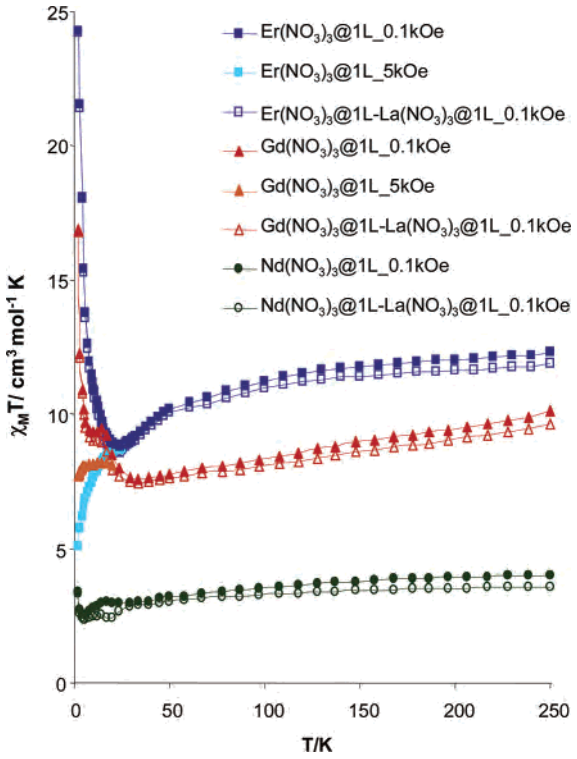

Figure 7. Field-cooled $\chi_M T$ versus T for the $\mathbf{NdNO_3@1_L}$, $\mathbf{GdNO_3@1_L}$, and $\mathbf{ErNO_3@1_L}$ species at 0.1 and 5 kG field strengths. The open symbols represent the $\mathbf{LnNO_3@1_L}$ $\chi_M T$ values subtracted from the $\mathbf{LaNO_3@1_L}$ ones. The continuous lines are a guide to the eye.

the metallacalix[4]arene. On the other side of the layer, the guest metal ions are coordinated by the four exocyclic oxygen atoms of the metallacalix[4]arene (consult Table 2 for $M-O_{pymo}$ distances), leading to Cu···M separations of about 4.40, 4.46, and 4.52 Å for K^+, Tl^+, and Rb^+, respectively. In the case of $\mathbf{KNO_3@1_L}$ and $\mathbf{RbNO_3@1_L}$, the coordination is further completed by the nitrate counterions and the water molecules. Each K^+ and Rb^+ ion is actually octacoordinated, with the four missing bond interactions being supplied by one water molecule, one monodentate nitrate, and one chelating nitrate. In completing the coordination of potassium and rubidium, the nitrate counterions bridge guest metal ions (8.29 and 7.94 Å apart, respectively) belonging to adjacent layers (Figures 3−4), thus determining a 3D network. The two distinct bridged distances, apparently anticorrelated to the different ionic radii of (octacoordinated) K^+ and Rb^+ ions (1.51 and 1.61 Å respectively),[8] suggest that the nitrate ion is a much weaker bridge in the former case, thus exalting the layered structure, as if the K^+ ions were only eptacoordinated. The "weakness" among consecutive layers in the potassium derivative might be considered to be responsible for the observed stacking defects (Experimental Section), resulting in a slightly different packing. (This is evidenced by the occurrence of monoclinic symmetry for $\mathbf{KNO_3@1_L}$. Such distortion, in principle, might be reversed in the upper layers of the ideal sequence, thus generating microtwinned, or polytypic, crystals, in agreement with the difficult sampling of the reciprocal space along *c**.)

A rather distinct situation is observed in the case of $\mathbf{TlNO_3@1_L}$, which, although being metrically isomorphous

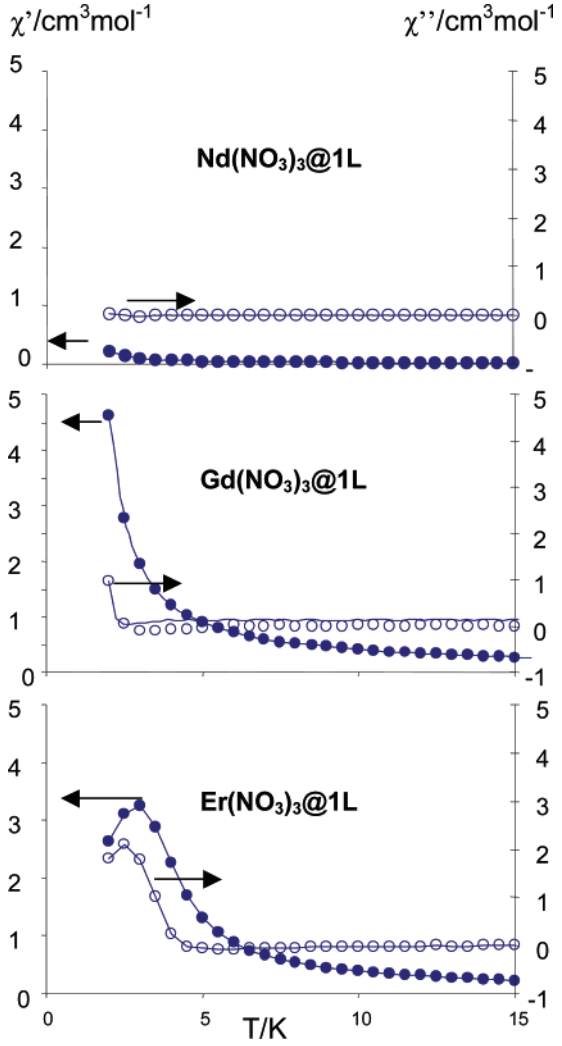

Figure 8. ac magnetic susceptibility measurements for the **$NdNO_3$@1$_L$**, **$GdNO_3$@1$_L$**, and **$ErNO_3$@1$_L$** species at 1 Oe and 100 Hz.

with **$RbNO_3$@1$_L$**, differs in the local geometry at the Tl^+ ion (r_{Tl+} = 1.59 Å for coordination number 8).[8] Actually, the latter appears to be only four-coordinated (Tl−O, 2.71(1)−2.84(1) Å), being bound to only the four exocyclic oxygen atoms of a metallacalix[4]arene moiety (Table 2). Neither water molecules (absent in the structure) nor nitrate ions (formally) increase its coordination number (Figure 5), with the shortest Tl−$O_{nitrate}$ contact falling above 3.1 Å.[16] This behavior can be traced back to the so-called "stereochemical activity" of its inert lone pair,[17] which is absent on K^+ and Rb^+. Accordingly, in the case of **$TlNO_3$@1$_L$**, the whole structure can be formally described (although with some idealization) by a (nitrate-filled) stacking of $[Cu(2\text{-pymo-}N1,N3)_2Tl]_n^+$ layers of the muscovitic type, that is, hosting oppositely charged (nearly unbound) ions.

X-ray Powder Diffraction Characterization of the $M(NO_3)_n$@1$_L$ Species Containing Di- and Trivalent Cations. Despite the poor crystallinity of the different species characterized by powder diffraction methods, unequivocal evidence can be gathered from the careful examination of the lattice parameters collectively reported in Table 3:

(i) Small divalent cations maintain the cubic symmetry of the anhydrous **1$_C$** phase or, better said, that of the hydrated small monovalent cations (Li^+, NH_4^+).[7] Be^{2+} and Mg^{2+} likely possess a significantly hydrated coordination shell, with water molecules extensively interacting through H bonds with the O atoms of the hexagonal windows of the sodalitic crystals. As expected, the lattice parameters for the Be^{2+} and Mg^{2+} derivatives are slightly larger (but surprisingly similar to each other) than those of the empty **1$_C$** framework (a_{Be} = 15.54

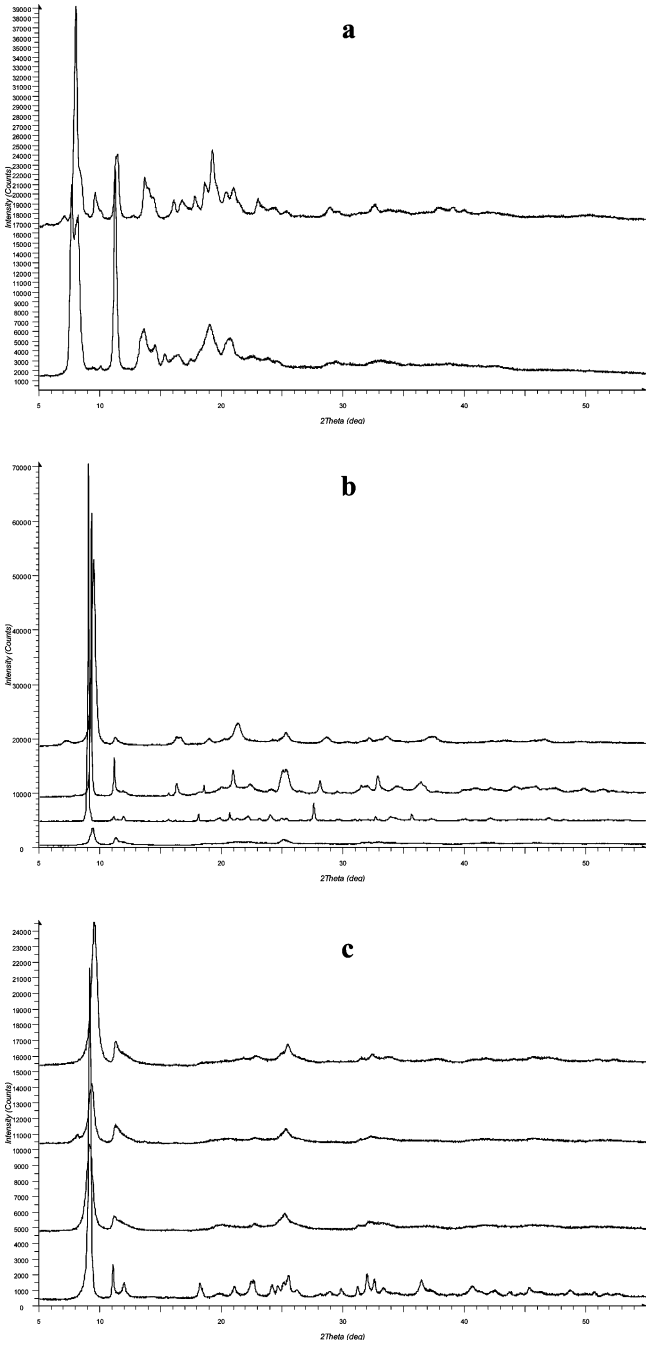

Figure 9. Raw diffraction data for the MNO_3@1$_L$ species: from top to bottom (a) Be, Mg; (b) Ca, Sr, Ba, Pb; and (c) Er, Gd, Nd, La. Horizontal axis: 2θ, deg. Vertical axis: counts.

(16) A CSD survey of TlO_4 fragments indicates the existence of two distinct populations for the Tl−O distances: one centered at about 2.38 Å and the other at 2.90 Å, both about 0.12 Å wide. Very rare indeed are Tl−O contacts greater than 3.1 Å, in agreement with our (idealized) description.

(17) Hueey, J. E.; Keiter, E. A.; Keiter, R. L. *Inorganic Chemistry*, 4th ed.; Harper Collins College Publisher: New York, 1993.

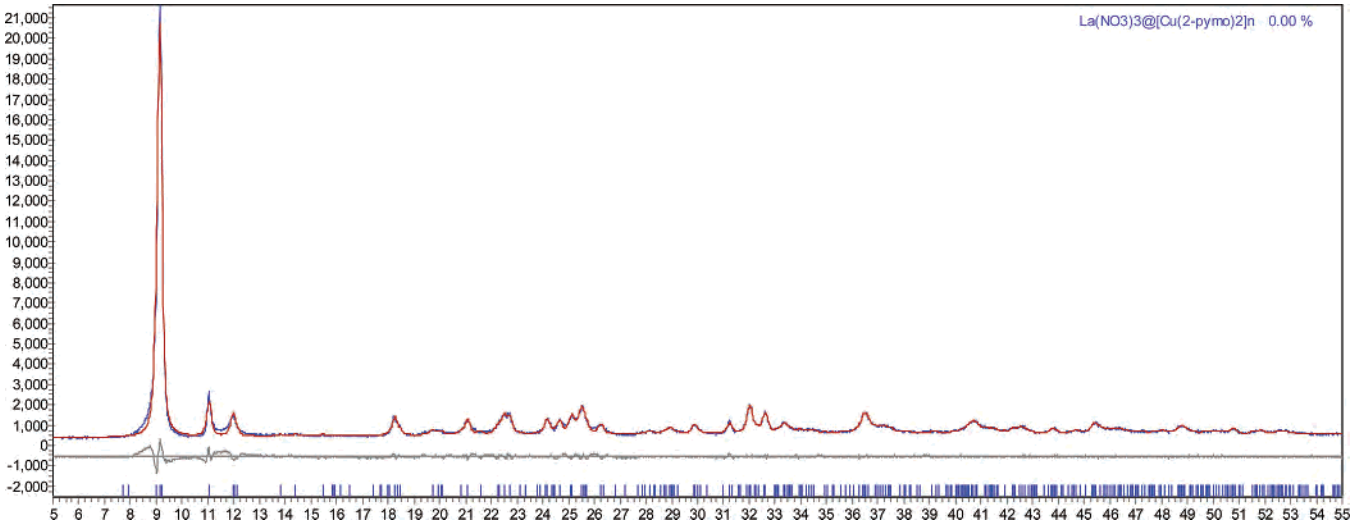

Figure 10. Le Bail plot (red) for the **La(NO$_3$)$_3$@1$_L$** species together with a difference plot (gray) and peak markers at the bottom. Horizontal axis: 2θ, deg. Vertical axis: counts.

Table 3. Crystal System, Le Bail Refined Cell Parameters, and M Ionic Radii for the **MNO$_3$@1** Species

M	crystal system	a (Å)	b (Å)	c, β (Å, deg)	V (Å^3)	r_{ion} (Å)[8]
Na	orthorhombic	11.06	11.66	18.33	2364	1.18[b]
Be	cubic	15.54			3755	0.27[a]
Mg	cubic	15.39			3647	0.57[a]
Ca	orthorhombic	11.02	11.38	18.60	2332	1.12[b]
Sr	orthorhombic	10.99	11.33	19.12	2383	1.26[b]
Ba	orthorhombic	11.26	11.38	19.27	2470	1.42[b]
Pb	monoclinic	10.61	11.65	19.69, 92.1	2434	1.29[b]
La	orthorhombic	11.17	11.44	19.22	2456	1.16[b]
Nd	orthorhombic	10.41	11.75	19.26	2363	1.11[b]
Gd	orthorhombic	10.55	11.38	19.00	2281	1.05[b]
Er	orthorhombic	10.79	11.22	18.48	2238	1.00[b]

[a] For coordination number 4. [b] For coordination number 8.

Å, a_{Mg}= 15.39 Å, a_{1C} = 15.07 Å). It is also noteworthy that the rhombohedral Be^{2+} and Mg^{2+} phases show a certain lattice variability, as recently observed for the **1$_R$** [Cu(2-pymo-*N*1,*N*3)$_2$]$_n$ frameworks, which contain a different number of water molecules [$V(Be^{2+})$ = 11 129 Å^3, $V(Mg^{2+})$ = 11 557 Å^3, V(**1$_R$**) = 11 517[7]−11 610[18] Å^3].

(ii) Larger divalent cations promote the formation of the layered **1$_L$** phase. The absence of a single-crystalline specimen can be interpreted by the need to accommodate, for electroneutrality reasons, twice as many nitrates, possibly disordered (and, perhaps, a few water molecules). The increase in the cell volumes clearly manifests the increase in the size of the metal ions in the Ca/Sr/Ba sequence, although the lattice expansion is clearly anisotropic. The Pb^{2+} species has been measured also, but because of its very poor crystallinity, it could not be described by an orthorhombic lattice.

(iii) Similarly to the divalent cations but to a larger extent, the rare earth derivatives show very broadened powder diffraction traces, aside from **LaNO$_3$@1$_L$**. In these species, a further disordering effect can be at work, which is related to the versatility and stereochemical flexibility of the Ln^{3+} ions, which are capable of sustaining a variety of coordination geometries and different hydration levels. Again, the increase in the ionic size for the Er^{3+}/Gd^{3+}/Nd^{3+}/La^{3+} sequence (from 0.88 to 1.02 Å) is manifested by the evident increase in the cell volume, which is mostly related to an inflation of the *c* axis, the stacking direction. Unlike divalent cations, it appears that in this class the species with the largest cation approaches tetragonality with a limited difference between the *a* and *b* axes (11.17 and 11.44 Å, respectively).

However, we note that, although clear, the trends reported above should not be taken as absolute because it is hard to address the correct periodicity (if any) in these highly defective species. It is likely that no matter which species is the most suitable choice for describing the observed patterns, the local geometry at the copper ions (well-characterized in a number of single-crystal specimens, here and in previous work) is maintained. Therefore, the structural diversity must be attributed to the guest ions (metal and nitrates) and water molecules, and it structurally strengthens the magnetic behavior discussion reported in the following section.

Magnetic Properties of the MNO$_3$@1$_L$ Species. The **MNO$_3$@1$_L$** materials show interesting magnetic properties. Their behavior can be divided into two different groups, the first one comprising the species with intercalated diamagnetic metal ions (i.e., K^+, Rb^+, Tl^+, La^{3+}) and the second one including the materials containing paramagnetic metal ions (Nd^{3+}, Gd^{3+}, Er^{3+}).

(i) Magnetism of MNO$_3$@1$_L$ (M = K$^+$, Rb$^+$, Tl$^+$, La^{3+}). The thermal behavior of the magnetic susceptibility χ_M, and that of $\chi_M T$, is very similar for all species. As a representative example, Figure 6 shows the results for **KNO$_3$@1$_L$**. In the high-temperature region, the thermal dependence of the magnetic susceptibility shows a smooth increase upon cooling down to ca. 80 K. At lower temperatures, χ_M smoothly decreases, reaching a minimum at about 40 K. Below this temperature, the χ_M values sharply increase and become dependent on the applied external field. Accordingly, in the high-temperature region, the $\chi_M T$ values steadily decrease upon cooling until the Néel temperature (T_N, about 35 K) is reached. At lower temperatures, the $\chi_M T$ values

(18) Barea, E.; Navarro, J. A. R.; Salas, J. M.; Masciocchi, N.; Galli, S.; Sironi, A., unpublished results.

Table 4. Main Magnetic Parameters for the $MNO_3@1_L$ Species (M = K, Rb, Tl, La)

M	g	J (cm^{-1})	ordering
K^+	2.091(3)	−63.1(2)	AF/WF
Rb^+	2.044(4)	−62.5(3)	AF/WF
Tl^+	2.06(1)	−54.1(9)	AF/WF
La^{3+}	2.07(1)	−56.5(9)	AF/WF

sharply increase and become field-dependent, with the curves' maxima lying around 19 K (Figure 6). The high-temperature behavior ($T > 40$ K) of these materials can be attributed to an efficient antiferromagnetic coupling of the copper(II) centers transmitted through the 2-pymo-*N*1,*N*3 exobidentate bridges. Each square-planar copper(II) center is connected to four other metal ions through pyrimidinolate bridges, defining a Heisenberg 2D square network of spins. Thus, in the 250−40 K range, the magnetic behavior of this series of materials can be conveniently described by eq 1, which is adequate for the description of the high-temperature dependence of the magnetic susceptibility on a 2D Heisenberg quadratic-layer antiferromagnet, where the spin Hamiltonian is defined as $H = \Sigma J S_i \cdot S_j$,[19] $\theta = kT/JS(S+1)$, g is the Landé g factor, μ_B is the Bohr magneton, and N is the number of spins in the lattice. The C_n coefficients[20] have been taken from ref 19.

$$\chi = \frac{Ng^2\mu_B{}^2}{J\left(3\theta + \sum_{n=1}^{\infty} \frac{C_n}{\theta^n - 1}\right)} \quad (1)$$

The best fit parameters, $g = 2.091(3)$ and $J = -63.1(2)$ cm^{-1}, are obtained for the magnetic data of $\mathbf{KNO_3@1_L}$ in the 250−40 K range. The coupling constants J of $\mathbf{RbNO_3@1_L}$, $\mathbf{TlNO_3@1_L}$, and $\mathbf{La(NO_3)_3@1_L}$ are similar (Table 4), which further agrees with their structurally related nature (above). The high (negative) J values found in this series are related to the square-planar geometry of the metal ions, which ensures a good overlap of the $d_{x^2-y^2}$ magnetic orbital with the orbitals of the bridging ligands, further confirming the efficiency of the pyrimidinolate bridges in transmitting magnetic interactions in polynuclear systems.[21] Nevertheless, the most interesting behavior is found in the low-temperature region ($T < 35$ K) when a clear change in the trend of the χ_M and $\chi_M T$ curves is observed. Our studies performed at different field strengths (1, 5, and 10 kOe, Figure 6) show an increment of the χ_M and $\chi_M T$ values at low fields, in agreement with a spin-canting phenomenon. The magnetization versus magnetic field measurements at 2 K give much lower values than the expected saturation value of $2\mu_B$[22] per $M(NO_3)_m[Cu(2\text{-pymo-}N1,N3)_2]_2$ formula unit (e.g., 0.06 μ_B for $\mathbf{La(NO_3)_3@1_L}$), which further agrees with weak ferromagnetic ordering arising from spin canting in an antiferromagnetic system.

Phenomenologically, all of these systems display an increase in $\chi_M T$ at $T < 35$ K. This is unequivocally a trace of a partial ordering of the spins at low temperature. However, because the $[Cu(2\text{-pymo-}N1,N3)_2]_n$ layers contain magnetically active centers and are centrosymmetric (described above), canting should be symmetrically forbidden. To match (room-temperature) crystallographic and (low-temperature) magnetic evidence, one of the following events (or both) might occur: (i) the structure at low temperature may be slightly distorted, through a structural (perhaps displacive) phase transition (which we cannot measure), or (ii) the magnetic lattice does not coincide with the crystallographic one. Indeed, magnetic domains may form because of the symmetry breaking that occurs during the magnetic ordering process.

(ii) Magnetism of $\mathbf{M(NO_3)_3@1_L}$ ($\mathbf{M = Nd^{3+}, Gd^{3+}, Er^{3+}}$). The thermal behavior of the magnetic susceptibility of the $\mathbf{Nd(NO_3)_3@1_L}$, $\mathbf{Gd(NO_3)_3@1_L}$, and $\mathbf{Er(NO_3)_3@1_L}$ materials has been measured in the 2−250 K temperature range at 100, 300, and 5000 Oe field strengths. The values of $\chi_M T$ versus T at 100 Oe are shown in Figure 7. The resulting magnetic behavior appears to be rather complex, which is consistent with the simultaneous operation of three distinct contributions: (i) the (intrinsically complex) magnetic behavior of the Ln^{3+} ions themselves, (ii) the magnetic behavior of the $[Cu(2\text{-pymo-}N1,N3)_2]_n$ layers, and (iii) further magnetic interactions involving the lanthanide ions. Reasonably, the observed magnetic behavior cannot be traced to Ln−Ln magnetic interactions because it is known that they are very weak and, in the present cases, also limited by the presence of nitrate anions, which are poor transmitting agents.[23]

For $\mathbf{Nd(NO_3)_3@1_L}$, the $\chi_M T$ product shows a steady decrease upon cooling to 30 K. Below this temperature, $\chi_M T$ smoothly rises, reaching a maximum of 3.02 $cm^3 \cdot mol^{-1}$ K at ca. 17 K. Below this temperature, $\chi_M T$ decreases again and eventually sharply increases below 5 K, reaching a value of 3.40 $cm^3 \cdot mol^{-1} \cdot K$ at 2 K. With the aim of clarifying the effect of intercalating the paramagnetic Nd^{3+} ion between the $[Cu(2\text{-pymo-}N1,N3)_2]_n$ layers, we have subtracted the $\chi_M T$ curve of $\mathbf{La(NO_3)_3@1_L}$ from that of $\mathbf{Nd(NO_3)_3@1_L}$ (Figure 7). In the high-temperature region, the subtracted $\chi_M T$ curve shows a smoother decrease upon cooling than the original $\mathbf{Nd(NO_3)_3@1_L}$ one, which might be attributed to the thermal depopulation of the Nd^{3+} Stark sublevels[6] after the antiferromagnetic contribution of the Cu-based layers has been erased. An additional effect of the subtraction of the $\mathbf{La(NO_3)_3@1_L}$ curve is the loss of the original maximum detected at ca. 17 K for the $\mathbf{Nd(NO_3)_3@1_L}$ system, a maximum that is therefore related to the same spin-canting phenomenon invoked for the layered $\mathbf{M(NO_3)_n@1_L}$ systems containing intercalated diamagnetic ions (previous paragraph). As the uncorrected curve, at temperatures below 5

(19) (a) Lines, M. E. *J. Phys. Chem. Solids* **1970**, *31*, 101. (b) Rushbrooke, G. S.; Wood, P. J. *Mol. Phys.* **1958**, *1*, 257.
(20) For $S = {}^1/_2$, the C_n coefficients take the values $C_1 = 4$, $C_2 = 2.667$, $C_3 = 1.185$, $C_4 = 0.149$, $C_5 = -0.191$, $C_6 = 0.001$.
(21) (a) Barea, E.; Navarro, J. A. R.; Salas, J. M.; Masciocchi, N.; Galli, S.; Sironi, A. *Polyhedron* **2003**, *22*, 3051. (b) Tabares, L. C.; Navarro, J. A. R.; Salas, J. M.; Willermann, M. *Inorg. Chim. Acta* **2001**, *318*, 166. (c) Barea, E.; Romero, M. A.; Navarro, J. A. R.; Salas, J. M.; Masciocchi, N.; Galli, S.; Sironi, A. *Inorg. Chem.* **2005**, *44*, 1472.
(22) Carlin, R. L. *Magnetochemistry;* Springer-Verlag: Berlin, 1986.
(23) Hendriks, H. M. J.; Birker, J. M. W. L.; Van Rijn, J.; Verschoor, G. C.; Reedijk, J. *J. Am. Chem. Soc.* **1982**, *104*, 3607.

K the subtracted $\chi_M T$ one shows an increase in $\chi_M T$ (to 3.31 $cm^3 \cdot mol^{-1} \cdot K$ at 2 K), which suggests a very weak ferromagnetic ordering taking place, possibly because of interactions of the Cu−Nd type. ac susceptibility measurements, performed in a 1 Oe field at 1−1000 Hz, further support a magnetic ordering taking place at very low temperatures, with the appearance of weak χ' and χ'' signals at 2 K (Figure 8).

With regard to the **$Gd(NO_3)_3$@1$_L$** and **$Er(NO_3)_3$@1$_L$** species, their magnetic behavior is dominated by the Ln^{3+} ions. Thus, in contrast to **$Nd(NO_3)_3$@1$_L$**, the subtraction of the **$La(NO_3)_3$@1$_L$** $\chi_M T$ curve from those of **$Gd(NO_3)_3$@1$_L$** and **$Er(NO_3)_3$@1$_L$** does not result in any significant change in their shape (Figure 7). In the high-temperature region, the $\chi_M T$ values of **$Er(NO_3)_3$@1$_L$** show a steady decrease upon cooling, down 25−30 K, which, as for the Nd^{3+} analogue, might be attributed to the thermal depopulation of the Stark sublevels. This effect is less pronounced in the **$Gd(NO_3)_3$@1$_L$** case, probably because the Gd^{3+} ions lack orbital angular momentum. Below 25 K, the $\chi_M T$ values for **$Gd(NO_3)_3$@1$_L$** sharply increase until a plateau is reached at 9.96 $cm^3 \cdot mol^{-1} \cdot K$, between 20 and 10 K. At lower temperatures, $\chi_M T$ rises again, reaching a value of 16 $cm^3 \cdot mol^{-1} \cdot K$ at 2 K. ac susceptibility measurements in a 1 Oe field at 1−1000 Hz support a ferromagnetic ordering taking place at low temperatures, with the appearance of a χ'' signal at $T < 3.5$ K (Figure 8). In the case of **$Er(NO_3)_3$@1$_L$**, the $\chi_M T$ values steadily increase at temperatures below 25 K, reaching a value of 24.3 $cm^3 \cdot mol^{-1} \cdot K$ at 2 K. As for the Gd^{3+} derivative, ac susceptibility measurements in a 1 Oe field at 1−1000 Hz (Figure 8), with the appearance of a χ'' signal at $T < 5$ K, support weak ferromagnetic ordering taking place at low temperatures, possibly due to ferromagnetic Cu−Er interactions.

It is known that coupled systems including at least one ion with orbital momentum are not amenable to quantitative analysis;[24] however, a conclusion can be extracted from the Nd^{3+}, Gd^{3+}, and Er^{3+} series.

Mainly, in the case of Nd^{3+} and Er^{3+}, the high-temperature behavior is dominated by the thermal depopulation of the Stark sublevels. At variance, in the low-temperature region, the behavior of the three species is distinct, depending on the nature of the Ln^{3+} metal ion. In the Nd^{3+} system, at very low temperatures (T about 2 K), a feeble ferromagnetic ordering is appreciated. In the case of Gd^{3+}, two different effects seem to be active: a first magnetic ordering below 20 K and a second one below 10 K. The effect at 20 K should probably be related to Cu−Gd ferromagnetic interactions transmitted through the pyrimidinolate bridges, whereas the second one probably arises from a longer-range magnetic ordering. Finally, for Er^{3+}, a ferromagnetic ordering seems to be present at temperatures below 25 K, which we also attribute to Cu−Er magnetic interactions transmitted through the O-bound pyrimidinolate bridges. From the above phenomenological observations, it might be concluded that the longer the radius of the lanthanide ions ($Nd^{3+} > Gd^{3+} > Er^{3+}$), the larger the unit-cell dimensions (Table 3) and the weaker the through-space and through-bond overlaps, hence the lower the ordering temperature.

We also performed field-dependent magnetization studies (at 2 K, 50 kOe), which afforded molar saturation magnetization values of 1.49μ_B, 6.90μ_B, and 2.83μ_B for the Nd^{3+}, Gd^{3+}, and Er^{3+} derivatives, respectively. Not surprisingly, these values are smaller than the saturated ones expected for free Ln^{3+} ions (i.e., 9μ_B, 7μ_B, and 9μ_B, for $M_{sat} = g_J J \mu_B$, in spin−orbit coupling approximation[25]). A similar behavior has indeed been already described in other Cu(II)−Ln(III) species and was attributed to crystal-field effects.[26]

Conclusions

We have presented a number of materials obtained upon incorporation of several metal nitrates in a layered copper pyrimidinolate framework, **1$_L$**. Such a heterogeneous solid−liquid process forces the reorganization of 3D open sodalitic species into 2D materials, the structural analogues of phyllosilicates. This interconversion occurs only for metal ions possessing ionic radii longer than 1.18 Å (for coordination number 8), whereas smaller cations (Li^+, Be^{2+}, and Mg^{2+}) maintain the cubic symmetry of the empty sodalite. A heterogeneous synthetic strategy for the preparation of heteronuclear polymeric metal complexes clearly differs from the classical approaches in the homogeneous phase using metal ligand precursors or compartmentalized ligands. Accordingly, the possibility of incorporating f-block metal ions within *predefined* crystalline materials opens the possibility of preparing novel molecular magnets, where the intrinsic magnetic properties of the lanthanides can be suitably modified through the ligand-mediated intermetallic interactions of the f and d ion sublattices.

We anticipate future work in preparing new layered species of this class, possibly employing d metal ions with a higher number of unpaired electrons and pyrimidinolate ligands substituted in the 5 position by halogens or nitro groups (X). This work aims at fine tuning the structural and functional properties of these materials, as recently proposed by our group for polymeric cobalt and zinc 5-X-pyrimidinolates (X = Cl, Br, I;[27] X = NO_2[21c]).

Acknowledgment. The Spanish Ministry of Education and Science (CTQ-2005-00329/BQU, EB postdoctoral grant (EX2005-1004)) and Junta de Andalucia are acknowledged for funding. The Fondazione Provinciale Comasca and Fondazione CARIPLO are thanked for partial financial support. We are indebted to the referees for providing very useful comments.

Supporting Information Available: X-ray single-crystal structures in CIF format for MNO_3@1L, (M = K^+, Rb^+, and Tl^+). This material is available free of charge via the Internet at http://pubs.acs.org.

IC061384I

(24) Costes, J. P.; Dahan, F.; Dupuis, A.; Laurent, J. P. *Chem.—Eur. J.* **1998**, *4*, 1616.
(25) Hatscher, S.; Schilder, H.; Lueken, H.; Urland, W. *Pure Appl. Chem.* **2005**, *77*, 497.
(26) Kido, Y.; Ykuta, Y.; Sunatsuki, Y.; Ogawa, Y.; Matsumoto, N. *Inorg. Chem.* **2003**, *42*, 398.
(27) Masciocchi, N.; Galli, S.; Sironi, A.; Cariati, E.; Galindo, M. A.; Barea, E.; Romero, M. A.; Salas, J. M.; Navarro, J. A. R.; Santoyo-González, F. *Inorg. Chem.* **2006**, *45*, 7612.